

Pinton, N., Grant, J. , Collins, S. and Cumming, D. R.S. (2018) Exploitation of magnetic dipole resonances in metal–insulator–metal plasmonic nanostructures to selectively filter visible light. *ACS Photonics*, 5(4), pp. 1250-1261. (doi:[10.1021/acsphotonics.7b00959](https://doi.org/10.1021/acsphotonics.7b00959))

This is the author's final accepted version.

There may be differences between this version and the published version. You are advised to consult the publisher's version if you wish to cite from it.

<http://eprints.gla.ac.uk/158280/>

Deposited on: 29 March 2018

Enlighten – Research publications by members of the University of Glasgow

<http://eprints.gla.ac.uk>

# Exploitation of magnetic dipole resonances in Metal-Insulator-Metal plasmonic nanostructures to selectively filter visible light

Nadia Pinton,<sup>\*,†,‡</sup> James Grant,<sup>‡</sup> Steve Collins,<sup>†</sup> and David R. S. Cumming<sup>‡</sup>

<sup>†</sup>*Department of Engineering Science, University of Oxford, Oxford*

<sup>‡</sup>*School of Engineering Science, University of Glasgow, Glasgow*

E-mail: [nadia.pinton@eng.ox.ac.uk](mailto:nadia.pinton@eng.ox.ac.uk)

## Abstract

Significant improvement in using plasmonic nanostructures for practical colour filtering and multispectral imaging applications is achieved by exploiting the coupling of surface plasmons with dielectric optical cavity resonances within a hexagonal array of subwavelength holes in a thin CMOS-compatible metal-insulator-metal stack. This polarisation-independent architecture overcomes the limitations of all previously reported plasmonic colour filters, namely poor transmission and broad band-pass characteristic, effectively providing a compact approach for high colour accuracy multispectral and filtering technologies. Measured transmission efficiencies up to 60% and full-width at half-maximum between 45 nm and 55 nm along the entire visible spectrum are achieved - an impressive and unique combination of features that has never been reported before. The nanostructure exploits the phenomenon of extraordinary optical transmission and magnetic dipole modes to efficiently filter visible light. The presence of magnetic resonances in the optical regime is an unusual property, previously reported in photonic metamaterials or dielectric nanoparticles. The physical insights

established from the electromagnetic near-field patterns are used to accurately tailor the optical properties of the filters. The non-ideality of the fabrication at the nanoscale is addressed, the issues encountered highlighted and alternative solutions proposed and verified, demonstrating that the working principle of the MIM structure can be successfully extended to other materials and structural parameters.

## Keywords

Surface Plasmon Polaritons, Plasmonics, 2D Periodic Array of Subwavelength Apertures, CMOS Image Sensors, Multispectral Imaging, Magnetic Dipole

The ability to selectively and efficiently filter light in the optical regime is of extreme importance in an increasingly wide range of applications. Visible band-pass optical filters are found in the photo/video cameras that we use daily: from smart phones, tablets, laptops, and gaming consoles to surveillance, automotive and medical systems. Commercial image sensors are usually based on the human eye colour acquisition, i.e. they utilise RGB filters to separate the incoming light into its main components so that a colour image can be digitally reconstructed. Multispectral sensors have demonstrated a higher colour accuracy,<sup>1,2</sup> a result of the separation of the optical spectrum in many colour channels instead of only three, which enable image analysis and machine vision beyond human capability. Multispectral imaging systems can also be used as a non-invasive approach to identify materials,<sup>3</sup> locate objects<sup>3</sup> or perform quality and safety diagnosis,<sup>4,5</sup> in particular when the application requires the acquisition of optical spectral information over only a few well-defined wavelengths of interest.

Recently, fully integrated megapixel snapshot multispectral cameras in the visible regime have been reported.<sup>6-8</sup> Traditional polymer-based filter technologies were replaced by all-dielectric multilayer stacks and the Bayer pattern extended to allow the simultaneous acquisition of multiple spectral bands without the need for external dedicated optics. However, despite the narrow passband of the stack filters, their implementation is costly and extremely

sensitive to process variations.

An alternative approach for multispectral filters consists of exploiting the ability of surface plasmon based nanostructures to control and manipulate light at the nanoscale.<sup>9–11</sup> Surface Plasmon Resonances (SPRs) are collective oscillations of surface charges that result from the coupling of incident photons with the coherent electron oscillations present in a conductor. They can be distinguished between localised electron oscillations and propagating evanescent waves depending on whether they are generated on metallic nanoparticles or along flat metal/dielectric interfaces, respectively. The latter are known as Surface Plasmon Polaritons (SPPs) and their contribution to the phenomenon of Extraordinary Optical Transmission (EOT)<sup>12</sup> is now widely accepted.<sup>9,10,13,14</sup>

The generation of colours through the engineering of metallic nanostructure is a rapidly growing research field and plasmonic colour nanotechnologies display great potential when compared to traditional colour technology.<sup>15</sup> Common applications range from colour printing and digital displays to optical sensing and security devices, and the structures of interest include diffraction gratings, nanoantennas, nanoaperture arrays and multilayer systems.<sup>15</sup> Bright colours have been demonstrated in reflection - for applications such as colour printing<sup>16</sup> - but the structure used is not suitable for image sensor applications. In the last decades, transmissive Plasmonic Colour Filters (PCFs) based on periodic arrays of nanoholes in an optically thick metal layer quickly became one of the most promising alternatives to polymer-based filter technologies for image sensors.<sup>13,17–19</sup> However, the relatively broad transmission passbands and relatively low transmission of these filters do not fulfil the requirements for multispectral imaging.

Recently, plasmonic nanostructures displaying band-pass spectral features potentially narrow enough to be used for spectral imaging have been proposed.<sup>20–23</sup> In 2008, a triplet of intersected bull’s eye structures and a combination of nanoslits with periodic grooves<sup>20</sup> were proposed to selectively filter the light in the visible regime. Despite full-widths at half-maximum (FWHM) of about 50 nm, both the structures lacked in transmission efficiency.



Absolute transmissions lower than 10-15% were achieved, probably a result of the high absorption losses of the thick silver layer. In 2010, Metal-Insulator-Metal (MIM) gratings<sup>21</sup> composed by a stack of Al-ZnSe-Al on top of a magnesium fluoride film were presented. However, these MIM grating structures<sup>21</sup> were only a slight improvement on standard single metal film nanohole arrays,<sup>18,19</sup> both in terms of transmission efficiency - that reached a maximum of 60% only for the green - and bandwidth - still greater than 100 nm. In fact, as a consequence of the poor colour selectivity, only 5 shades of colour are clearly distinguishable in the so-called *plasmonic spectroscope* proposed. In 2017, Fleischman *et al.*<sup>22</sup> described how by stacking two MIM gratings on top of each other to create a multilayer slot-mode plasmonic filter (MSPF) composed of 5 alternating layers of Ag and SiO<sub>2</sub> it could be possible to achieve colour filters with single transmission band as narrow as 17 nm and  $\approx 40\%$  peak transmission. Experimental prototypes with a FWHM of 70 nm were demonstrated. Nonetheless, all the above structures<sup>20-22</sup> are polarisation dependent, do not use standard CMOS-process materials, and cannot be integrated within a standard microchip because they exploit the air environment to operate. Finally, unprecedented experimental linewidth of  $\approx 80$  nm and transmission efficiency above 40% have been achieved in the NIR when some of the circular apertures in the unit cell of thin Au hexagonal nanohole arrays were substituted with ellipses.<sup>23</sup> The nanostructure exhibits polarisation insensitivity, however, Au is neither a CMOS compatible material or suitable to filter light in the blue and green parts of the visible spectrum.

Here, we report the design, the structural parameter analysis and experimental measurements of a plasmonic MIM array of subwavelength nanoholes. This can be embedded in a dielectric environment and easily integrated on top of an image sensor. The nanostructure displays high transmission efficiencies and narrow passbands along the entire visible regime, overcoming the limitations of all previously reported plasmonic filters. Insights into the physical mechanisms of the transmission process are established from the electric and magnetic near-field patterns, which indicate that the nanoholes behave like dielectric optical cavity

resonators. This demonstrates that the MIM filters exploit magnetic resonances at optical frequencies, an unusual property previously reported in structures such as photonic metamaterials<sup>11,24–26</sup> or dielectric nanoparticles.<sup>11,27–30</sup> Finally, an extensive user-friendly guideline for a successful optimisation of the nanostructure for specific applications is provided and insightful information on some of the most common nanofabrication processes are obtained from the high resolution electron micrographs. The MIM plasmonic filters are an extremely versatile technology that paves the way to monolithically integrate PCFs in commercial CMOS image sensors for high colour accuracy filtering and multispectral applications.

## Results and discussion

Figure 1a presents the schematic top view (i) and cross-section (ii) of the proposed MIM architecture, in comparison with the cross-sections (iii)<sup>31</sup> and (iv)<sup>18,19</sup> of two previously reported configurations based on periodic hexagonal nanohole arrays. Their transmission characteristics have been simulated (see *Methods* section for details) and the results are presented in Figure 1b. A significant improvement in bandwidth results from the increase in refractive index (RI) of the hole filling material (from configuration (iv) to (iii) and (ii)). Moreover, the addition of a second top thin metallic layer in the MIM structure (from configuration (iii) to (ii)) greatly reduces the transmission efficiency of the second broad peak at longer wavelengths - which is almost of the same magnitude as the first narrower resonance in configuration (iii) - and strongly compromises the passband characteristics of the filter, causing optical colour cross-talk in particular between the blue and red part of the visible spectrum.<sup>31</sup>

Previous studies<sup>10,32</sup> have demonstrated that when the propagation constant of SPPs,  $k_{\text{SPP}}$ , (Equation (1)) matches the reciprocal vectors  $G_{ij}$  given by the periodicity of the array (Equation (2)) minima in transmission appear, ascribed to the spectral location of Wood-Rayleigh anomalies. The transmission maxima, or EOT peaks, appear then red-

shifted in wavelength. In Figure 1b, the minimum  $\lambda_{\min,1}$  at approximately 490 nm, occurring in all the configurations, appears in concomitance with the matching of the condition  $k_{\text{SPP}(\text{Al}/\text{SiO}_2)}(\omega) = G_{10}$  and it is in fact related to the SPPs at the bottom aluminium/silicon dioxide (substrate) interface. Similarly, the presence of an aluminium/silicon nitride (Al/Si<sub>3</sub>N<sub>4</sub>) interface causes the appearance of a second transmission minimum, at longer wavelengths. Its position can be calculated as described in the *Supporting Information*.

Physical insights can be obtained from the electric and magnetic near-field patterns. Figure 2 displays the squared amplitude of the electric and magnetic fields at the transmission maxima, in the XZ-plane and YZ-plane respectively, for the three configurations. The full set of electric and magnetic fields at the transmission maxima in the XY-plane, YZ-plane and also in three XY-planes, including their respective x-, y- and z- components can be found in the *Supporting Information* for each of the three architectures. In Figures 2a and 2b, a clear confinement of either the magnetic or the electric field suggests that the nanoholes behave like dielectric optical cavity resonators. For the MIM and Aym-(thin)SML designs, the two identifiable maximum peaks in transmission are caused by magnetic dipoles (MDs) in the YZ-plane,  $\lambda_{\text{res}1}$ , and electric dipoles (EDs) in the XZ-plane,  $\lambda_{\text{res}2}$ . The appearance of magnetic and electric resonant modes in subwavelength dielectric resonators (DRs) at visible frequencies has been successfully demonstrated in several studies, from dielectric nanoparticles<sup>28-30,33</sup> to dielectric resonators nanoantennas.<sup>34</sup>

Usually, electromagnetic (EM) confinement in DRs arises from a large difference in permittivity, of the order of tens of units,<sup>34,35</sup> between the material that composes the resonator and the dielectric environment. Moreover, the resonance of isolated DRs is solely given by their structural parameters. However, in this case, the confinement of the fields is sustained by the presence of metal at the sidewalls of the holes and the resonant wavelength depends strongly on the coupling of SPRs. Consequently, the resonant modes are given by a collective response of the nanoholes and shift in wavelength with the periodicity  $a_x$  of the array,

which in turn provides the matching condition for the SPP excitations, and establishes the polarisation of the charges and, as a result, also the near- electric field pattern within the nanostructure.

The MD mode is characterized by an electric displacement current loop, which induces an orthogonally-oriented magnetic dipole moment.<sup>29,30</sup> The current loop requires opposite orientation of the electric field along  $z$ , and thus can only exist when there is enough retardation of the  $E_x(z)$  field between the cavity extremities.<sup>29</sup> In contrast, the ED mode originates from the collective polarisation of the nanoholes in response to an external driving field, parallel to the polarisation of the electric field. A magnetic current loop is then induced by the oscillating ED. This current loop can also extend outside the dielectric cavity, enabling the ED mode to exist even when the cavity is too short to support the MD mode. Clearly, the resonant wavelength of the modes depends on the optical length of the cavity.

Knowing that a resonance within a cavity occurs when its length is an integral number of half-wavelength of the wave,<sup>29,34–36</sup> we can approximate the effective optical length of a cavity mode as  $h_{\text{eff}} \approx \alpha \lambda_{\text{res}} / (2n)$ , where  $\alpha$  is an integer larger than zero,  $\lambda_{\text{res}}$  is the resonant wavelength and  $n$  is the RI of the cavity. As in the case of DRs or a slab waveguide,<sup>35</sup> the higher the RI of the core material with respect the cladding, the higher the degree of confinement and thus the shorter the effective optical length of the mode. This effect can be observed in Figure 2, where the MIM and Asym-SML architectures clearly display a higher degree of confinement of the fields at resonances. In the Sym-SML case, the magnetic field extends into both the silicon dioxide substrate and cap layer, which results in an optically thicker cavity. This means that the resonances of all three structures appear in the same wavelength range despite the difference in RI of the cavity material.

The identification of magnetic and electric dipoles at resonances is extremely interesting for the development of the plasmonic filters. Above the first-order transmission minimum  $\lambda_{\text{min}}|_{@k_{\text{SPP}}(\omega)=G_{10}}$ , the transmission of the array is given by the superposition of the magnetic and electric dipoles contributions. This insight makes it possible to control these two physical

phenomena and thus to optimise the transmission properties of a nanohole array for a specific application by tailoring the choice of geometrical and material parameters. Figure 3 contains a set of simulation results and shows the dependence of the MIM transmission efficiency on its main structural parameters. This data was used as a guideline to identify an optimum geometry for the fabrication of the samples.

By increasing the diameter of the holes it is possible to increase the transmission efficiency of the band-pass filter (Figure 3a). At the same time, the larger the diameter, the broader the linewidth. Nonetheless, even at the largest value of diameter used, the maximum FWHM is approximately 75 nm, which is still 25% narrower than the FWHM of the Sym-SML nanohole arrays filters (see Figure 1b), while the maximum transmission is greater than 70%. As expected, because the effective length of the cavity mode - given by the retardation of the  $E_x(z)$  - remain constant, the MD resonant peak displays good stability to variations in hole diameter.

Figures 3b and 3c show the dependence of the filtering characteristics of the MIM design on the presence of a  $\text{SiO}_2$  or a  $\text{Si}_3\text{N}_4$  cap layer, respectively. As stated before, the difference in RI between the hole filling material and the environment provides the degree of confinement along  $z$ . In fact, a  $\text{SiO}_2$  cap layer does not significantly affect the filter behaviour. In contrast, when the cap layer matches the hole filling material, the effective length of the cavity increases. As a consequence, the MD resonance red-shifts and higher order modes are allowed inside the cavity. A similar behaviour can be observed when increasing  $t_{\text{stack}}$  for three different periodicities  $a_x$  (see Figure 3d, 3e and 3f). In fact, for a given RI, the ratio  $\lambda_{\text{res}}/h_{\text{eff}}$  is constant and thus a thicker optical cavity corresponds to a longer resonant wavelength, and vice versa.

To limit the lithography to a single step, a constant  $t_{\text{stack}}$  for all the filters is preferable. Figure 3g displays the transmission efficiencies for a selected set of structural parameters and represents the chosen target for the nanofabrication. For a  $t_{\text{stack}} = 150$  nm and a fixed periodicity to diameter ratio of 1.53, the structure exhibits an almost constant transmission

efficiency above 60% and FWHM of the order of 50-60 nm along the entire optical visible range. Moreover, a 10 nm variation in periodicity corresponds to a 10 nm step in wavelength between adjacent peaks. MIM filters can therefore be easily designed to accurately target a desired working wavelength.

## Experimental results

The nanofabrication process has been divided in two main phases: patterning of the hexagonal nanohole arrays through the MIM stack and filling of the holes. Figure 4a depicts the steps for the first phase of the nanofabrication process, which are described in detail in the *Methods* section. After step (v), common practice would be to remove the  $\text{Si}_3\text{N}_4$  hard mask, used as an adhesion layer between the top aluminium layer and the resist. However, Figure 4b shows that the additional  $\text{Si}_3\text{N}_4$  etching step causes a considerable amount of under-etch of the  $\text{Si}_3\text{N}_4$  middle layer and thus this step was not executed in the subsequent samples.

Herein, we present the experimental results of six  $300\text{ }\mu\text{m} \times 300\text{ }\mu\text{m}$  MIM hexagonal nanohole arrays with different periodicities. Each array was optically characterized by means of a Scanning Electron Microscope (SEM) and a Microspectrophotometer. The SEM image in Figure 4c shows that each nanohole is composed by two concentric circles with a top,  $d_t$ , and a bottom,  $d_b$ , diameter. This means that the nanoholes in the bottom aluminium layer are slight smaller than the nanoholes in the top aluminium layer, by approximately 40 nm, and thus that the sidewalls of the holes are not perfectly vertical. However, the top surface of the arrays appears free from resist residuals and the holes are nicely circular-shaped.

Figure 4d displays the measured transmission characteristics of one of the arrays in comparison with the simulated transmission efficiencies of three possible sidewall configurations, indicated in the inset. The ideal sidewall (i) can be ruled out by Figure 4c and thus the simulation results with a sidewall of the (iii)-type are the best fit for this particular sample. Therefore, the (iii)-type sidewall profile is used to fit the remaining 5 squares with differing periodicities (see Figure 4e). The good agreement of the simulated results with the

experimental data is reflected by the high-quality matching of the critical features in the transmission spectra.

The second phase of the fabrication, illustrated in Figure 5a, consists of filling the nanohole arrays with  $\text{Si}_3\text{N}_4$ . After the  $\text{Si}_3\text{N}_4$  deposition, the optical characterization of the samples did not show the expected results. The TEM image of the cross-section of one of the samples in Figure 5b shows that if the hard mask is left in situ, the under-cut of the middle layer is avoided. However, the  $\text{Si}_3\text{N}_4$  deposition is highly non-conformal. A large void is visible inside each nanohole, a consequence of the mushroom-shaped accumulations between the holes that prevent complete filling. The experimental data of the sample whose cross-section is displayed in the TEM image are reported in the *Supporting Information*. The presence of the void interferes strongly with the filters' transmission by lowering the effective RI of the hole and thus decreasing  $h_{\text{eff}}$ . As a result, the MD mode disappears while the ED mode blue-shifts significantly. These unexpected difficulties in fabrication necessitated the identification of an alternative material to fill the holes.

Figure 5c shows the simulated transmission efficiencies as a function of the RI of the material inside the holes, for a constant  $t_{\text{stack}}$ . As expected, both the modes red-shift as the RI increases and the MD dipole resonance appears only when the cavity becomes optically thick enough to sustain the mode. Moreover, the lower the RI of the filling material the stronger the overlap of the modes, in particular when the RI is lower than the RI of the substrate. Noticeably, as previously reported in subwavelength apertures,<sup>37</sup> increasing the RI of the filling material increases the transmission. However, the higher the RI the wider the bandwidth of the MD resonance. In spite of this, increasing the RI improves the performance of the structure as band-pass filter. Based upon these results and the knowledge that a spinnable material could reduce the possibility of non-uniform filling and of an irregular top surface, the S1805 Shipley resist was chosen as the hole filling material.

The RI of S1805 is in the range 1.6-1.7,<sup>38</sup> lower than the RI of  $\text{Si}_3\text{N}_4$ , and thus, to maintain the optical length, the total  $t_{\text{stack}}$  of the MIM filters was increased. Figure

5d displays the final expected transmission characteristics using S1805 hole filling instead of  $\text{Si}_3\text{N}_4$ , for several periodicities  $a_x$  and a taller  $t_{\text{stack}} = 180$  nm. In this case, it appears that it is not possible to utilize the same thickness to uniformly filter the entire visible spectrum. The chosen thickness  $t_d = 100$  nm optimises the transmission efficiency in the middle range of the visible spectrum, but gives inferior passband characteristics in the blue and red part of the spectrum, which would require instead a shorter and a longer stack thickness, respectively. This is due to the fact that, for the first mode,  $\delta h_{\text{eff}} \approx \delta \lambda / (2n)$ , and thus, given the fixed wavelength range of visible light, a lower RI material requires a larger variation of the thickness  $\delta h_{\text{eff}}$ . Therefore, by filling the holes with a high-RI dielectric, narrowband filters can be realized across the entire visible spectrum with a single  $t_{\text{stack}}$  thickness.

The fabrication steps and experimental results of 40nm-100nm-40nm MIM hexagonal nanohole arrays filled with S1805, having different periodicities and exposed to different doses, are reported in Figure 6. As previously, following the SEM characterization of the top surface of the sample, the experimental measurements were compared to simulated results to determine the best fit for the hole sidewall profiles (see Figure 6b). Figure 6c shows that after the S1805 spin, the thickness of the resist on top of the MIM structure was of the order of around 100 nm. As in the case of the  $\text{SiO}_2$  cap, etching back the resist decreases the optical length of the cavity. As expected, when the S1805 top layer is etched back the peaks blue-shifts in wavelength and only a smaller number of modes are allowed inside the cavity, i.e. the second longer wavelength peak disappears (see Figure 6d).

The experimental results of two sets of the 40nm-100nm-40nm arrays after 40 minutes  $\text{O}_2$  back etching, that were exposed to two different doses as indicated, are plotted in Figures 6e and 6f. For the lower dose (Figure 6f), which corresponds to smaller hole diameters, the colour cross-talk between filters is evidently lower when compared to the higher doses (see insets). On the other hand, the transmission efficiency is significantly reduced by using the lower dose. In fact, for the higher dose, the sample displays transmission efficiencies up



to 60%, and FWHM in the blue and green part of the spectrum between 45 and 55 nm. The experimental results are in very good agreement with the simulations, establishing the accuracy and validity of the simulation study with  $\text{Si}_3\text{N}_4$  hole filling.

## Conclusions

Through a detailed set of simulation studies and the high quality of measured results obtained from the fabricated samples, we were able to demonstrate the impressive performance and versatility of our MIM plasmonic nanostructures. The MIM filters overcome the limitations of both existing PCFs and CMOS focal plane colour filters, and thanks to a reduced optical bandwidth down to as little as 45 nm in the visible range, and transmission efficiencies up to 60%, high accuracy image sensors will be made possible. Moreover, because these narrow band-pass filters for the entire visible range are fabricated using one single lithographic step, this CMOS-compatible plasmonic nanostructure is cost-efficient and extremely competitive with current multispectral filtering technologies.

We have established that the transmission spectrum, above the first-order transmission minimum  $\lambda_{\min}|_{@k_{\text{SPP}}(\omega)=G_{10}}$ , is dominated by the superposition of magnetic and electric resonant modes. This insight, and the understanding of the impact that the effective cavity length has on the magnetic dipole mode, has been successfully used to accurately tailor the choice of geometrical and material parameters of the nanohole array, and, therefore, to control the physical performance of the design and optimise the transmission characteristics of the filters for a specific application. The observed magnetic and electric dipole resonances resemble the optical properties of photonic metamaterials and dielectric nanoresonators. They establish that the MIM nanostructure enables a subwavelength confinement inside the nanoholes so that the system behaves as an array of interactive dielectric optical cavity resonators coupled to surface plasmon resonances.

Further improvements of the MIM filters will require a more reliable fabrication process,

so that a higher refractive index material can be used to fill the holes and a lower colour cross-talk achieved between the blue and the red part of the spectrum. However, when we optimised the MIM structure to a different hole filling material in just few steps, we clearly demonstrated that the concept presented in this manuscript is extremely versatile, and can be successfully extended to other materials or even to other wavelengths of the electromagnetic spectrum.

## Methods

**SPPs dispersion relation: flat metal/dielectric interface.** For a TM-polarized wave (E-field parallel to the interface), the surface plasmon polaritons dispersion relation  $k_{\text{SPP}}$  for a flat interface between a metal and a dielectric, assumed non-magnetic ( $\mu = 0$ ) and having permittivity  $\epsilon_m$  and  $\epsilon_d$  respectively, is given by:

$$k_{\text{SPP}} = k_0 \sqrt{\frac{\epsilon_d \epsilon_m}{\epsilon_d + \epsilon_m}} \quad \text{with} \quad n_{\text{SPP}} = \sqrt{\frac{\epsilon_d \epsilon_m}{\epsilon_d + \epsilon_m}} \quad (1)$$

where  $\mathbf{k}_0$  is the wavevector of the light in free space and  $n_{\text{SPP}}$  is the SPPs refractive index.

From the condition of surface waves excitation, the essential requirement for the existence of surface plasmon polaritons is for the interface to be composed of two materials with dielectric functions opposite in sign, such as a metal,  $\epsilon_m < 0$ , and a dielectric,  $\epsilon_d > 0$ . Since the term under the square root has to be positive,  $\epsilon_d + \epsilon_m$  has to be negative and thus the absolute value of the metal permittivity must be larger than the absolute value of the dielectric one, i.e.  $|\epsilon_m| > |\epsilon_d|$ . It follows then that the SPPs wavevector is larger than the wavevector of the incident light and therefore additional momentum is required to meet the boundary condition for the conservation of momentum at the interface and thus to excite the surface plasmon resonances. Considering a fixed metal  $\epsilon_m$ , the higher the permittivity of the dielectric at the interface, the larger the SPPs propagation constant.

**SPPs coupling in 2-D periodic arrays of subwavelength holes.** Diffraction from the sharp edges of individual subwavelength holes in a metal layer can provide the extra momentum required to generate SPPs.<sup>10,13</sup> However, in the case of a periodic array of holes the additional momentum required to observe EOT is provided by the periodicity of the array. The condition to be satisfied is  $k_{\text{SPP}} = k_{\parallel} + G_{ij}$ , where  $k_{\parallel} = k \sin \theta$  is the component of  $\mathbf{k}$  parallel to the interface and  $G_{ij}$  is the reciprocal vector of the periodic array. For normal incidence,  $\theta = 0$  and thus  $k_{\text{SPP}} = G_{ij}$ . For a hexagonal lattice with period  $a_x$ , the additional momentum is given by:

$$G_{ij} = \frac{4\pi}{a_x\sqrt{3}}\sqrt{i^2 + j^2 + ij} \quad (2)$$

where  $i$  and  $j$  are integers (with  $i \geq 0, j > 0$ ) and indicate the diffraction orders. It follows that the wavelengths  $\lambda_{\text{min}}$  at which the transmission minima are predicted to occur are given by:

$$\lambda_{(i,j)} = \frac{2\pi}{G_{ij}} n_{\text{SPP}}|_{@k_{\text{SPP}}(\omega)=G_{ij}} = \frac{\sqrt{3}a_x}{2\sqrt{i^2 + j^2 + ij}} n_{\text{SPP}}|_{@k_{\text{SPP}}(\omega)=G_{ij}} \quad (3)$$

**Numerical simulations.** Simulations of the transmission spectra were carried out with a high performance 3D Finite-Difference Time-Domain (FDTD) method Maxwell solver from Lumerical Solutions (*FDTD Solutions*). Incident light is simulated with a plane wave source that covers a wavelength range of 350 to 800 nm, placed within the silicon dioxide substrate. Only normally incident light is considered and thus both the polar and azimuthal angles of propagation, *theta* and *phi*, respectively, are set to zero. Polarisation angle is set to zero to define TM radiation. A single unit of the array is modelled, and symmetric/antisymmetric boundary conditions for the fields, consistent with the source's polarisation, are used. This reduces the simulation volume by 4. Periodic boundary conditions are set in the x-y plane and perfect absorbing layer conditions are used along z to eliminate/reduce the possibility of multiple reflection at the top and bottom boundaries of the simulation volume. An override 3D mesh is added in the metal layer (that covers all the 3 layers for the MIM structure).

The mesh accuracy was set to 0.5 nm. The silicon dioxide and aluminium layers use the “*SiO<sub>2</sub> (Glass) - Palik*” and “*Al (aluminium) - Palik*” models included in the default material database, respectively. The silicon nitride layer was added to the database as  $(n,k)$  *Material* by uploading a 3-column file containing wavelength, and the corresponding real (n) and imaginary part (k) of its refractive index, respectively. The file was downloaded in 2014 from the *PhotonicsDB: Optical Constants* research tool, hosted on the *nanoHUB* website.

**Samples fabrication.** Fabrication steps of the nanohole arrays have been divided into 2 main phases, (I) the nanohole patterning of the arrays and (II) the hole filling. Devices have been fabricated on top of glass substrate, in order to allow the optical characterisation of the filters in transmission. Substrates were bought from *MicroChemicals*: 15 x 15 mm borosilicate pieces, 2-side polished and a thickness of about  $500 \pm 25 \mu\text{m}$ . Phase I of the fabrication is illustrated in Figure 4a. It starts with the sequential deposition of the three layers that compose the MIM structure: in sequence, aluminium, silicon nitride, and aluminium, respectively. The values of the thicknesses of the metal and silicon nitride of each sample are indicated in the text. An additional silicon nitride film of 20 nm (or 10 nm according to the sample) is deposited on top of the structure. This layer is needed to improve the adhesion of the resist on top of the structure. A 2:1 dilution of *ZEP520A* resist to anisole is then spun on the substrate, baked at 180 °C and then exposed. After the development of the resist, samples are ready for dry etch. A sequential 4-step plasma reactive ion etching (RIE) process reproduces the e-beam patterns in the underlying layers. Finally, the remaining ZEP on top of the structure is removed and the samples are optically characterised. The silicon nitride hard mask was not removed because a strong under-etch of the middle layer was identified in the samples that went through its dry etch removal (see Figure 4b). Phase II of the fabrication consists in the filling of the nanohole arrays, more specifically with silicon nitride, as depicted in Figure 5a. The planned fabrication method included (a) the deposition of a thick layer of silicon nitride by PECVD to fill the holes. A thick layer

is supposed to reduce the steps at the nanoholes sidewalls given by the difference in height, (b) a slow chemical-mechanical polishing or RIE back-etching of the silicon nitride up to the top aluminium using an interferometer, and last (c) a silicon dioxide cap layer deposition. Unfortunately, the optical characterization of the samples after the silicon nitride deposition did not show the expected results and a cross-section of one of the sample revealed that the problem lay in the silicon nitride deposition itself (see Figure 5b). A second phase was then developed to fill the holes with a different type of material, in this case the S1805 resist, as represented in Figure 6a and described in detail in the dedicated section below.

**Metal deposition.** Metal deposition was performed by means of an electron beam evaporator, *Plassys MEB 550S* or *Plassys MEB 400S*. Both the tools have a cryo pumped load lock and main chamber, a 10kW electron beam source, and uses the same type of 99.99999% aluminium in the source. Deposition rate was set at 0.3 nm/s. The working pressure during evaporation was around  $1 \times 10^{-6}$  torr.

**Silicon nitride deposition.** Silicon nitride deposition was performed using Inductively Coupled Plasma Enhanced Chemical Vapour Desposition (ICPECVD) (*Oxford Instrument System 100 ICP 180 PECVD*). This is a high density plasma tool for room temperature deposition of low stress silicon nitride (breakdown voltage of  $4 \times 10^6$  V/cm for 5-nm thick films).

**Electron-beam lithography.** A 2:1 dilution of high resolution positive tone electron beam resist ZEP520A (formulated by *ZEON Chemicals L.P.*) to anisole was spin-coated onto the samples. Spin rate: 2250 rpm for 60 seconds. Average measured film thickness: 230-250 nm. Bake: oven at 180 °C for 40 minutes. EBL was performed using a *Vistec VB6 UHR EWF* electron beam lithography system with an electron voltage of 100kV. Samples were developed in a 99% O-xylene solution for 35 seconds, rinsed by immersion in IPA for 30 seconds and then blow-dried with Nitrogen. The samples were then placed for 30 seconds in

an *Oxygen Barrel Asher* to remove residuals of the resist prior to dry etching.

**Dry etching.** Silicon nitride dry etching was performed using a combination of Reactive Ion Etching (RIE) tools: *Oxford Instruments System 100 RIE T-gate* for the 20-nm  $\text{Si}_3\text{N}_4$  hard mask layer and *Oxford Instruments RIE 80+* for the middle layer. The recipes used were  $\text{SF}_6 / \text{N}_2 = 25/50 \text{ sccm}$ , 75 W, 30 mTorr, and  $\text{CHF}_3 / \text{Ar} = 25/18 \text{ sccm}$ , 200 W, 30 mTorr, respectively. Interferometer reading was used to determine the etching step duration. Aluminium dry etching was performed using a Reactive Ion Etching (RIE) tool, *Oxford Instruments System 100 RIE T-gate*. Recipe:  $\text{SiCl}_4 = 18 \text{ sccm}$ , 250 W, 9 mTorr. Samples were submerged in water right after the removal of the sample from the vacuum chamber to remove residuals of chloride and avoid the formation of oxide on the Al surfaces.

**S1805 Hole Filling.** S1805 resist is spun on the arrays after the dry etching steps. Spin rate: 9000 rpm for 60 seconds. Range of measured film thicknesses on top of the arrays: 100-150 nm. Samples were baked on a hot plate at 100-120 °C for around 5 minutes to remove the solvent component from the resist. Etch-back of the resist was performed with an *Oxygen Barrel Asher* at 100 W in sequential steps of 10 minutes each, which resulted in a etching rate of about 25 nm every 10 minutes.

**High-resolution imaging.** The fabricated arrays were imaged using a *FEI Nova NanoSEM 630* Scanning Electron Microscope (SEM). Acceleration voltage: 10 kV. Working distance: 5.5 mm. Detector: Through the Lens Detector (TLD). Mode: Secondary Electrons (SE). Cross-sections of the samples were cut by mean of a *DualBeam Focussed Ion Beam* (FIB) System and imaged with a Transmission Electron Microscope (TEM) at the Kelvin Nanocharacterization Centre facilities (*School of Physics and Astronomy, University of Glasgow*).

**Optical Characterization.** The optical properties of the hexagonal nanohole arrays were

measured in transmission mode using a *Foster+Freeman ffTA/MS Microspectrophotometer*. The instrument was calibrated before each recording with an optical transmission filter manufactured from glass doped with a mixture of rare-earth elements (Didymium = Neodymium + Praseodymium), as described in the manual. Data was collected with unpolarised halogen-bulb light, colour temperature 6000K, wavelength range 400 nm to 1000 nm (no IR blocking filter). Illumination was set to brightfield mode at normal incidence. Collimator was used to ensure collimated light was hitting the surface of the arrays. An objective lens with a optical magnification of 4.0X and numerical aperture (NA) of 0.25 was used for the optical characterization of the samples.

Figure 1: **From broad- to narrow-band plasmonic colour filters.** (a) Top view (i) of a hexagonal nanohole array and cross-sections for three different configurations of plasmonic filters on half-space  $\text{SiO}_2$  substrates: (ii) *MIM*: a metal-insulator-metal stack of  $\text{Al-Si}_3\text{N}_4\text{-Al}$ , holes filled with  $\text{Si}_3\text{N}_4$ ; (iii) *Asym-(thin)SML*: a thin Al layer capped with a  $\text{Si}_3\text{N}_4$  layer, holes filled with  $\text{Si}_3\text{N}_4$ ; (iv) *Sym-SML*: a thick Al layer capped with a  $\text{SiO}_2$  layer, holes filled with  $\text{SiO}_2$ . (b) Comparison of the transmission efficiencies of the MIM structure with the Asym-(thin)SML and Sym-SML designs. MIM:  $t_m = 40$  nm,  $t_d = 60$  nm, no cap. Asym-(thin)SML:  $t_m = 40$  nm,  $t_{\text{cap}} = 100$  nm. Sym-SML:  $t_m = 150$  nm,  $t_{\text{cap}} = 200$  nm. For all the structures: periodicity  $a_x = 380$  nm and diameter  $d = 210$  nm. The introduction of a high-refractive index material results in a narrow passband feature, while the addition of a second metallic layer, an exact copy of the bottom one, greatly reduces the transmission of the broad peak at longer wavelengths and thus the optical colour cross-talk. The minimum  $\lambda_{\text{min},1}$  coincides with the matching of the condition  $k_{\text{SPP}(\text{Al}/\text{SiO}_2)} = G_{10}$  (refer to *Supporting Information*).

Figure 2: **Magnetic and electric dipoles at optical wavelengths.** Squared amplitudes of the electric and magnetic fields at resonances, in the XY-plane and YZ-plane respectively, for the (a) MIM, (b) Asym-(thin)SML and (c) Sym-SML structures. The white arrows in the background represent the electric and magnetic vectors potential, respectively. The orange and blue circles represent electric and magnetic current loops, respectively. The yellow and blue thick lines represent electric and magnetic dipoles, respectively. The MIM and Asym-(thin)SML structures show a clear confinement of either the magnetic,  $\lambda_{\text{res},1}$ , or electric,  $\lambda_{\text{res},2}$  field, which corresponds to a magnetic or electric dipole respectively. They display a higher degree of confinement of the modes along  $z$  due to the higher difference in RI between the hole filling material and the substrate/cap layers. In fact, in the Sym-SML case, the fields can extend inside the substrate and cap layers, which are composed by the same material of the hole filling, and thus the effective length of the cavity modes is larger. Full set of fields for each configuration, including their x-, y- and z- components, can be found in the *Supporting Information*.



**Figure 3: Simulation study to analyse the dependence of the optical transmission of the MIM structure on its structural parameters.** (a) Influence of the size of the nanoholes. The larger the diameter the higher the transmission efficiency. The MD resonance is stable to diameter variations.  $a_x = 380$  nm,  $t_m = 40$  nm,  $t_d = 60$  nm, no cap. (b), (c) Influence of the thickness of a  $\text{SiO}_2$  and a  $\text{Si}_3\text{N}_4$  cap layer, respectively.  $a_x = 380$  nm,  $d = 250$  nm,  $t_m = 40$  nm,  $t_d = 60$  nm. A  $\text{SiO}_2$  cap layer does not significantly affect the filter behaviour. In contrast, when the cap layer matches the hole filling material, the cavity length increases as  $t_{\text{stack}} + t_{\text{cap}}$ . As a consequence, the MD resonance red-shifts and higher order modes are allowed inside the cavity. (d), (e), (f) Influence of the total stack thickness  $t_{\text{stack}}$  (by varying the thickness of the middle dielectric layer,  $t_m = 40$  nm stays constant) for three different periodicities ( $a_x$  equals to 280 nm, 380 nm and 480 nm, respectively) The periodicity to diameter ratio has been kept constant, i.e.  $d = a_x/1.53$  nm. No cap. For a given RI, the ratio  $\lambda_{\text{res}}/h_{\text{eff}}$  is constant and thus a thicker optical cavity corresponds to a longer resonant wavelength, and vice versa. (g) Optimised MIM structure. A uniform transmission efficiency above 60% and FWHM of 50-60 nm can be obtained along the entire visible range for  $d = a_x/1.53$  nm.  $t_m = 40$  nm,  $t_d = 70$  nm,  $t_{\text{cap},\text{SiO}_2} = 50$  nm.

**Figure 4: Lithographic patterning of the hexagonal nanohole arrays.** (a) Illustration of the fabrication steps used to pattern the hexagonal nanohole arrays in the 3-layer MIM stack. Detailed information on each of the steps can be found in the *Methods Section*. (b) Sketch of the cross-section within the hexagonal array and respective TEM image (sample S21940) of the MIM stack in between two consecutive nanoholes along the x-direction. The removal of the hard mask results in a significant under-etch of the  $\text{Si}_3\text{N}_4$  middle layer. Scale bar: 20 nm. (c) SEM image of Square 4 (sample S23800) after the last step (v) of the first phase of the PCFs nanofabrication. Two circumferences, one at the bottom Al layer ( $d_b$ ) and one at the top Al layer ( $d_t$ ), can be identified. That means that the sidewalls of the nanoholes are not perfectly vertical. Scale bar: 400 nm. (d) Optical transmission of Square 4 (sample S23800). Sidewall (i) indicates the ideal case. In case (ii), it is assumed that the  $\text{Si}_3\text{N}_4$  middle layer has been etched up to the top hole dimension, while in case (iii) a uniformly stepped sloped sidewall is considered. Excluding the ideal case (i) which is ruled out by Figure 4c, sidewall (iii) is the best parametric fitting. (e) Optical transmission efficiency of the six  $300 \times 300 \mu\text{m}$  arrays of sample S23800 (solid lines) after the last step of Phase I of the nanofabrication in comparison with the fitted simulation results (dashed lines). Structural parameters used in the simulations are listed in the *Supporting Information*, under the section dedicated to the sample S23800. Experimental measurements are in very good agreement with the simulated results.

Figure 5: **Optimization of the structure for a different hole filling material.** (a) Illustration of the fabrication steps to fill the holes with  $\text{Si}_3\text{N}_4$ . (b) Sketch of the cross-section within the hexagonal array and respective TEM image of one of the fabricated arrays (sample S23801 - see dedicated section in the *Supporting Information*). The deposition displays non-conformality, with a higher deposition rate on the top surface which creates mushroom-shape accumulations at the side of the nanoholes that do not allow complete filling of the subwavelength apertures. Scale bar: 200 nm. (c) Simulation study for the replacement of  $\text{Si}_3\text{N}_4$  as hole filling material: the transmission varies as a function of the RI of the material inside the nanoholes.  $a_x = 380$  nm,  $d = 250$  nm,  $t_m = 40$  nm,  $t_d = 70$  nm, no cap. A 10-nm  $\text{Si}_3\text{N}_4$  hard mask is assumed. The structure shows a change of behaviour when the refractive index inside the holes becomes higher than silicon dioxide. Noticeably, for the same value of stack thickness, the higher the refractive index of the material inside the holes the higher the transmission. Moreover, the higher the refractive index the lower the colour cross-talk of the ED. (d) Expected optical transmission efficiency for 40-100-40 MIM arrays having different periodicities  $a_x$  (indicated on top of the peaks). The periodicity to diameter ratio is 1.53,  $t_m = 40$  nm,  $t_d = 100$  nm, no cap. A 10-nm  $\text{Si}_3\text{N}_4$  hard mask is assumed. The chosen thickness  $t_d = 100$  nm optimises the transmission efficiency in the middle range of the visible spectrum, but gives inferior passband characteristics in the blue and red part of the spectrum, which would require instead a shorter and a longer stack thickness, respectively.

Figure 6: **Experimental results for the S1805 nanohole filling.** (a) Illustration of the fabrication steps used to fill the holes with S1805. A 10-nm  $\text{Si}_3\text{N}_4$  hard mask was used. (b), (c), (d), (e), and (f) Optical characterisation of Sample S24734:  $t_m = 40$  nm,  $t_d = 100$  nm, 10-nm hard mask. Each array occupies an area of  $200 \mu\text{m} \times 200 \mu\text{m}$ . See the dedicated section in the *Supporting Information* for details of the sample layout and measured hole dimensions. Measured transmission efficiencies of square 11,  $a_x = 380$  nm, E-beam dose  $408 \mu\text{C}/\text{cm}^2$ , sample S24734 (b) after Phase I of the fabrication process in comparison with parameterised simulations curves having different hole sidewalls, (c) after S1805 spin in comparison with simulated results having different cap thickness, and (d) as a function of the S1805 cap thickness after 10-minute steps of  $\text{O}_2$  back-etching. (e) Comparison of measured transmission efficiencies (solid lines) of the arrays of sample S24734 exposed to a dose of  $408 \mu\text{C}/\text{cm}^2$  with the simulation results (dashed lines) obtained using a (ii)-type hole sidewall and the diameters obtained from the SEM characterisation of each array. Periodicities are indicated on top of the peaks. Inset: transmission microscope image of the 16 MIM colour filters, periodicities are indicated at the top of each square. Experimental results are in good agreement with the simulation curves. (f) Measured transmission efficiencies of the arrays of sample S24734 exposed to a dose of  $300 \mu\text{C}/\text{cm}^2$ . Periodicities are indicated on top of the peaks. Inset: transmission microscope image of the 16 MIM colour filters, periodicities are indicated at the top of each square.

## Supporting Information Available

The Supporting Information file contains:

- The theory to evaluate the SPP dispersion relation for the case of a single flat interface and a single slab of arbitrary dielectric constant to show the correlation between minima in transmission and the matching of the SPP propagation constant  $k_{\text{SPP}}$  with the additional wavevector  $G_{ij}$  of the periodic array.
- Simulation data to confirm the polarisation independence of the MIM structure.
- Electric and magnetic near-field patterns at the transmission maxima in the XY-plane, YZ-plane and XY-planes, and their respective x-, y- and z- components for each of the three configurations presented in the manuscript.
- E-beam design layouts, spectral characterisation and SEM characterisation of the fabricated MIM plasmonic filter arrays presented in the manuscript.

## Author Information

### Corresponding Author

E-mail: nadia.pinton@eng.ox.ac.uk

### ORCID

Nadia Pinton: 0000-0003-1072-5534

### Notes

The authors declare no competing financial interest.

## Acknowledgements

The authors thank the technical staff of the James Watt Nanofabrication Centre at the University of Glasgow for the assistance in fabricating the devices reported in this paper. This work is supported by the European Commission (EU) under the Initial Training Network Marie-Curie Scheme (EDISON-GA project).

## References

- (1) Burns, P. D.; Berns, R. S. Analysis Multispectral Image Capture. *Proc. Colour and Imaging Conference* **1996**, 4, 19-22.
- (2) Yamaguchi, M. et al. Color image reproduction based on multispectral and multiprimary imaging: experimental evaluation. *Proc. SPIE* **2001**, 4663, 15-23.
- (3) Shaw, G. A.; Burke, H. K. Spectral imaging for remote sensing. *LLabJ* **2003**, 14, 3-28.
- (4) Wu, D.; Sun, D. Advanced applications of hyper spectral imaging technology for food quality and safety analysis and assessment: a review - Part II: applications. *IFSET* **2013**, 19, 15-28.
- (5) Fawzy, Y. S.; Zeng, H. Spectral imaging technology - A review on skin and endoscopy applications. *Recent Pat. Med. Imaging* **2014**, 4, 101-109.
- (6) Eichenholz, J. M.; Barnett, N.; Juang, Y.; Fish, D.; Spano, S.; Lindsley, E.; Farkas, D. L. Real-time megapixel multispectral bioimaging. *Proc. SPIE* **2010**, 7568, 75681L.
- (7) Tack, N.; Lambrechts, A.; Soussan, P.; Haspeslagh, L. A compact, high-speed and low-cost hyperspectral imager. *Proc. SPIE* **2012**, 8266, 82660Q.
- (8) Geelen, B.; Tack, N.; Lambrechts, A. A compact snapshot multispectral imager with a monolithically integrated per-pixel filter mosaic. *Proc. SPIE* **2010**, 8974, 89740L.
- (9) Kik, P. G.; Brongersma, M. L.; Surface Plasmon Nanophotonics In *Surface Plasmon Nanophotonics*; Brongersma, M. L., Kik, P. G., Eds.; Springer series in Optical Sciences: Netherlands, 2007; pp 1-10.
- (10) Garcia-Vidal, F. J.; Martin-Moreno, L.; Ebbesen, T. W.; Kuipers, L. Light passing through subwavelength apertures. *Rev. Mod. Phys.* **2010**, 82, 729-787.
- (11) Jahani, S.; Jacob, Z. All-dielectric metamaterials. *Nat. Nanotech.* **2016**, 11, 23-36.

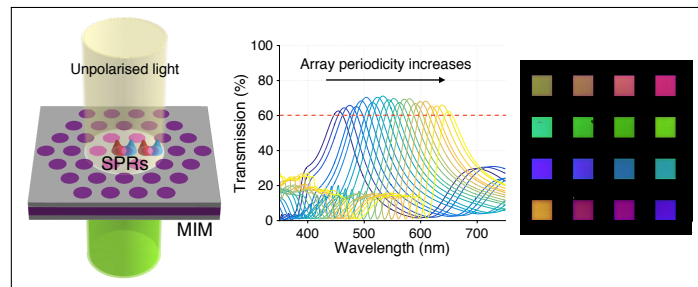
- (12) Ebbesen, T. W.; Lezec, H. J.; Ghaemi, H. F.; Thio, T.; Wolff, P. A. Extraordinary optical transmission through sub-wavelength hole arrays. *Nature* **1998**, 391, 667-669.
- (13) Genet, C.; Ebbesen, T. W. Light in tiny holes. *Nature* **2007**, 445, 39-46.
- (14) García de Abajo, F. J. Colloquium: Light scattering by particle and hole arrays. *Rev. Mod. Phys.* **2007**, 79, 1267-1290.
- (15) Kristensen, A.; Yang, J. K. W.; Bozhevolnyi, S. I.; Link, S.; Nordlander, P.; Halas, N. J.; Mortensen, N. A. Plasmonic colour generation. *Nat. Rev. Mater.* **2016**, 2, 16088.
- (16) Flauraud, V.; Reyes, M.; Paniagua-Domínguez, R.; Kuznetsov, A. I.; Brugger, J. Silicon nanostructures for bright field full color prints. *ACS Photonics* **2017**, 4, 1913-1919.
- (17) Catrysse, P. B.; Wandell, B. A. Integrated color pixels in 0.18- $\mu\text{m}$  complementary metal oxide semiconductor technology. *J. Opt. Soc. Am. A* **2003**, 20, 2293-2306.
- (18) Chen, Q.; Das, D.; Chitnis, D.; Walls, K.; Drysdale, T. D.; Collins, S.; Cumming, D.R.S. A CMOS image sensor integrated with plasmonic colour filters. *Plasmonics* **2012**, 7, 695-699.
- (19) Burgos, S. P.; Yokogawa, S.; Atwater, H. A. Color imaging via nearest neighbor hole coupling in plasmonic color filters integrated onto a complementary metal-oxide semiconductor image sensor. *ACS Nano* **2013**, 7, 10038-10047.
- (20) Laux, E.; Genet, C.; Skauli, T.; Ebbesen, T. W. Plasmonic photon sorters for spectral and polarimetric imaging. *Nat. Photon.* **2008**, 2, 161-164.
- (21) Xu, T.; Wu, Y.; Luo, X.; Guo, L. J. Plasmonic nanoresonators for high-resolution colour filtering and spectral imaging. *Nat. Commun.* **2010**, 1, 59.
- (22) Fleischman, D.; Sweatlock, L. A.; Murakami, H.; Atwater, H. Hyper-selective plasmonic color filters. *Optics Express* **2017**, 25, 27386-27395.

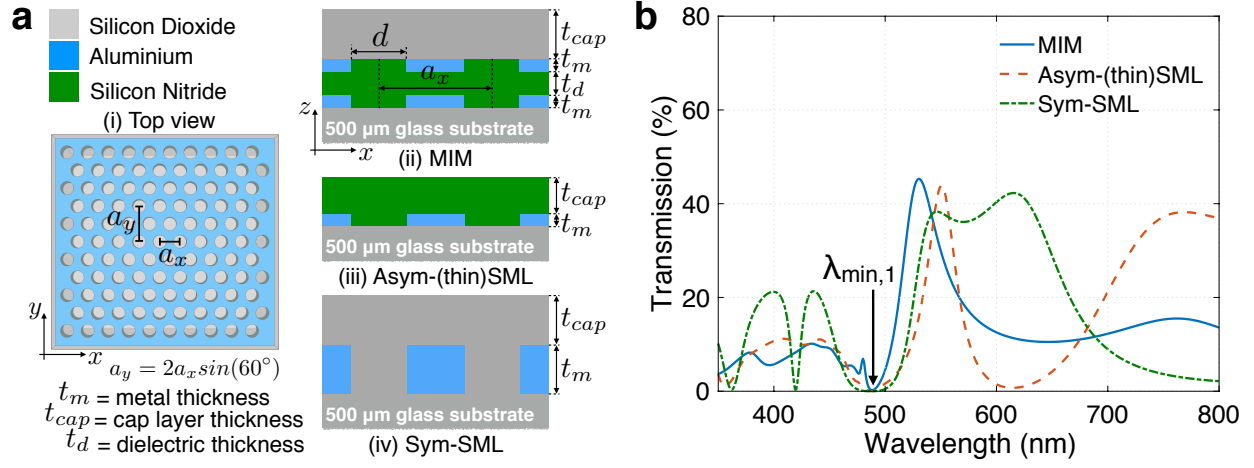
- (23) Shah, Y. D.; Grant, J.; Hao, D.; Kenney, M.; Pusino, V.; Cumming, D. R. S. Ultra-narrow line width polarization-insensitive filter using a symmetry-breaking selective plasmonic metasurface. *ACS Photonics* **2017**.
- (24) Ahmadi. A.; Mosallaei, H. Physical configuration and performance modeling of all-dielectric metamaterials. *Phys. Rev. B - Condens. Matter Mater. Phys.* **2008**, 77, 045104.
- (25) Luk'yanchuk, B.; Zheludev, N. I.; Maier, S. A.; Halas, N. J.; Nordlander, P.; Giessen, H.; Chong, C. T. The Fano resonance in plasmonic nanostructures and metamaterials. *Nat. Mater.* **2010**, 9, 707-715.
- (26) Soukoulis, C. M.; Wegener, M. Past achievements and future challenges in the development of three-dimensional photonic metamaterials. *Nat. Photon.* **2011**, 5, 523-530.
- (27) Peng, L.; Ran, L.; Chen, H.; Zhang, H.; Kong, J. A.; Grzegorzczuk, T. M. Experimental observation of left-handed behaviour in an array of standard dielectric resonators. *Phys. Rev. Lett.* **2007**, 98, 157403.
- (28) Evlyukhin, A. B.; Novikov, S. M.; Zywiets, U.; Eriksen, R. L.; Reinhardt, C.; Bozhevolnyi, S. I.; Chichkov, B. N. Demonstration of magnetic dipole resonances of dielectric nanospheres in the visible region. *Nano Lett.* **2012**, 12, 3749-3755.
- (29) Van De Groep, J.; Polman, A. Designing dielectric resonators on substrates: combining magnetic and electric resonances. *Opt. Express* **2013**, 21, 26285-26302.
- (30) Van De Haar, M. A.; Van De Groep, J.; Brenny, B. J. M.; Polman, A. Controlling magnetic and electric dipole modes in hollow silicon nanocylinders. *Opt. Express* **2016**, 24, 2047-2064.
- (31) Pinton, N.; Grant, J.; Choubey, B.; Cumming, D.; Collins, S. Recent progress in plasmonic colour filters for image sensor and multispectral applications. *Proc. SPIE* **2016**, 9884, 988438.

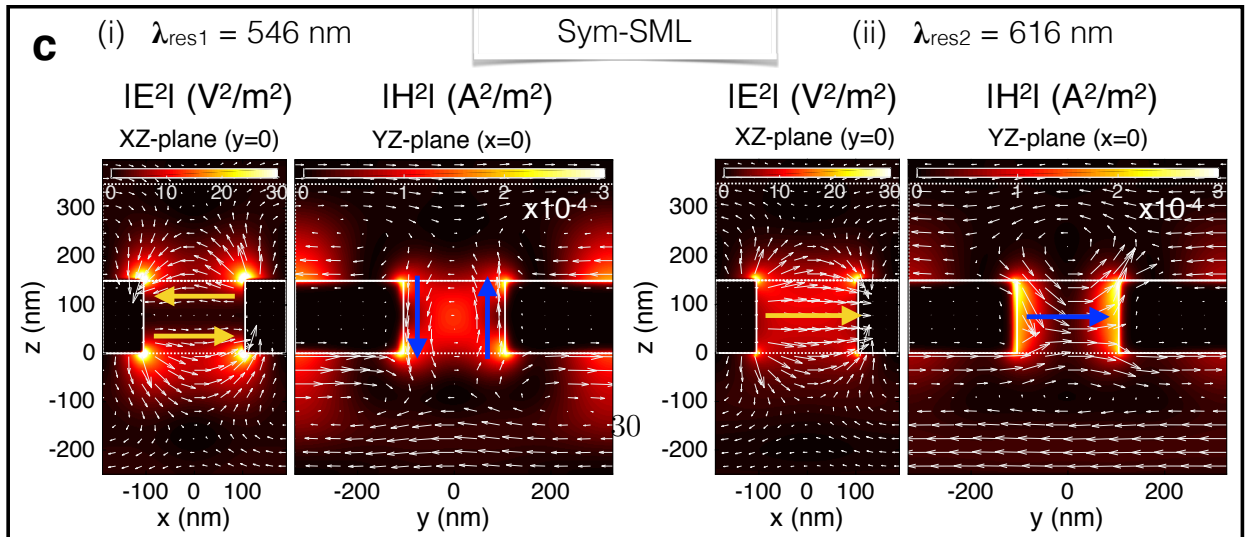
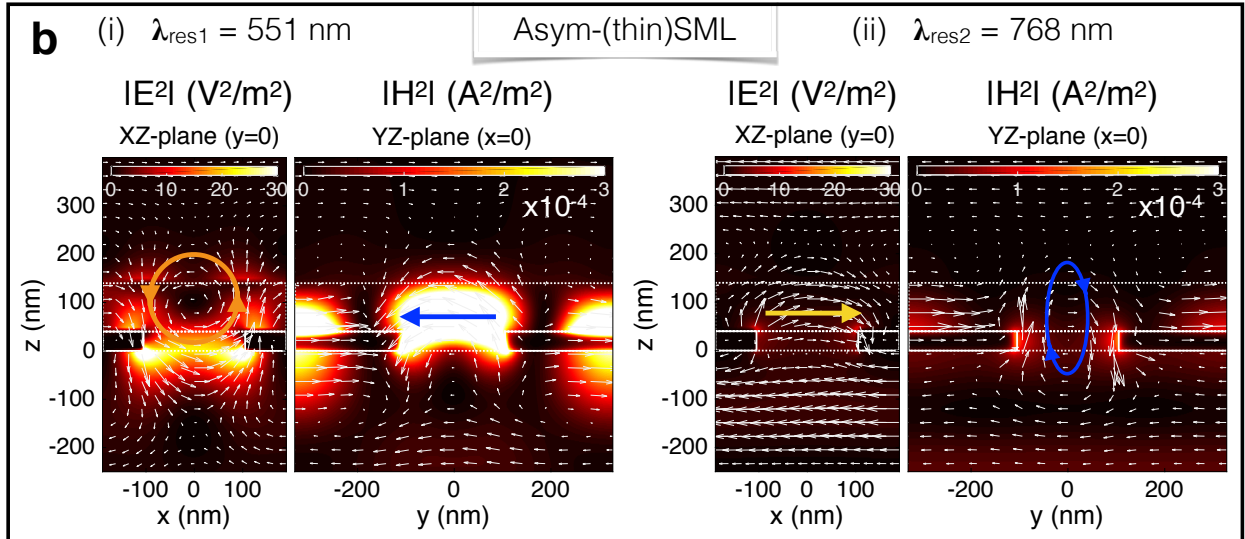
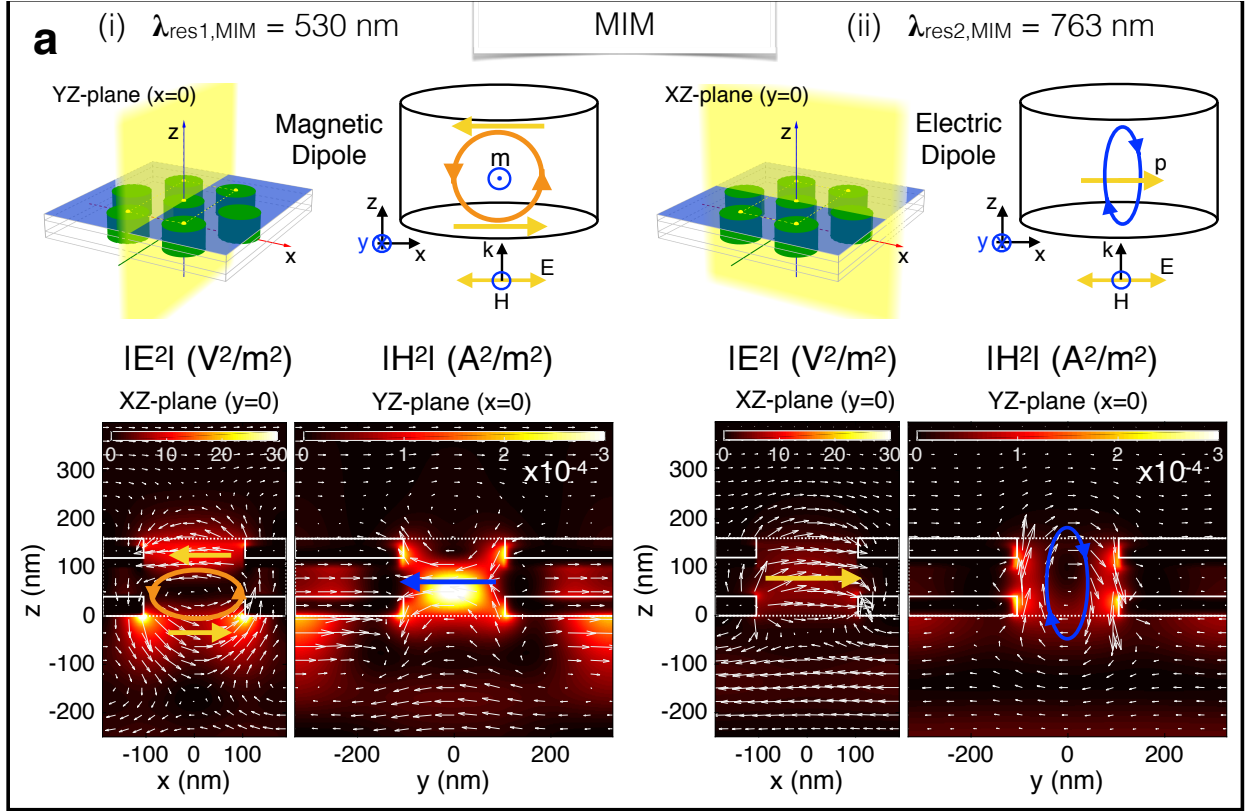
- (32) Pacifici, D.; Lezec, H. J.; Sweatlock, L. A.; Walters, R. J.; Atwater, H. A. Universal optical transmission features in periodic and quasiperiodic hole arrays. *Opt. Express* **2008**, 16, 9222-9238.
- (33) Staude, I.; Miroshnichenko, A. E.; Decker, M.; Fofang, N. T.; Liu, S.; Gonzales, E.; Dominguez, J.; Luk, T. S.; Neshev, D. N.; Brener, I.; Kivshar, Y. Tailoring directional scattering through magnetic and electric resonances in subwavelength silicon nanodisks. *ACS Nano* **2013**, 7, 7824-7832.
- (34) Kajfez, D.; Kishk, A. A. Dielectric resonator antenna-possible candidate for adaptive antenna arrays. *Proc. VITEL, Next Gener. Netw. Beyond* **2002**, 13-14.
- (35) Balanis, C. A. *Advanced Engineering Electromagnetics* Wiley: New York, 2007; pp 351-541.
- (36) Kobayashi, Y.; Tanaka, S. Resonant modes of a dielectric rod resonator short-circuited at both ends by parallel conducting plates. *IEEE Trans. Microw. Theory Tech.* **1980**, 28, 1077-1085.
- (37) García de Abajo, F. J. Light transmission through a single cylindrical hole in a metallic film. *Opt. Express* **2002**, 10, 1475-1484.
- (38) Dow Shipley Microposit S1800 series photo resists. <http://micromaterialstech.com/products/gi-line-broadband-photoresists/dow-shipley-s1800-photoresist/>

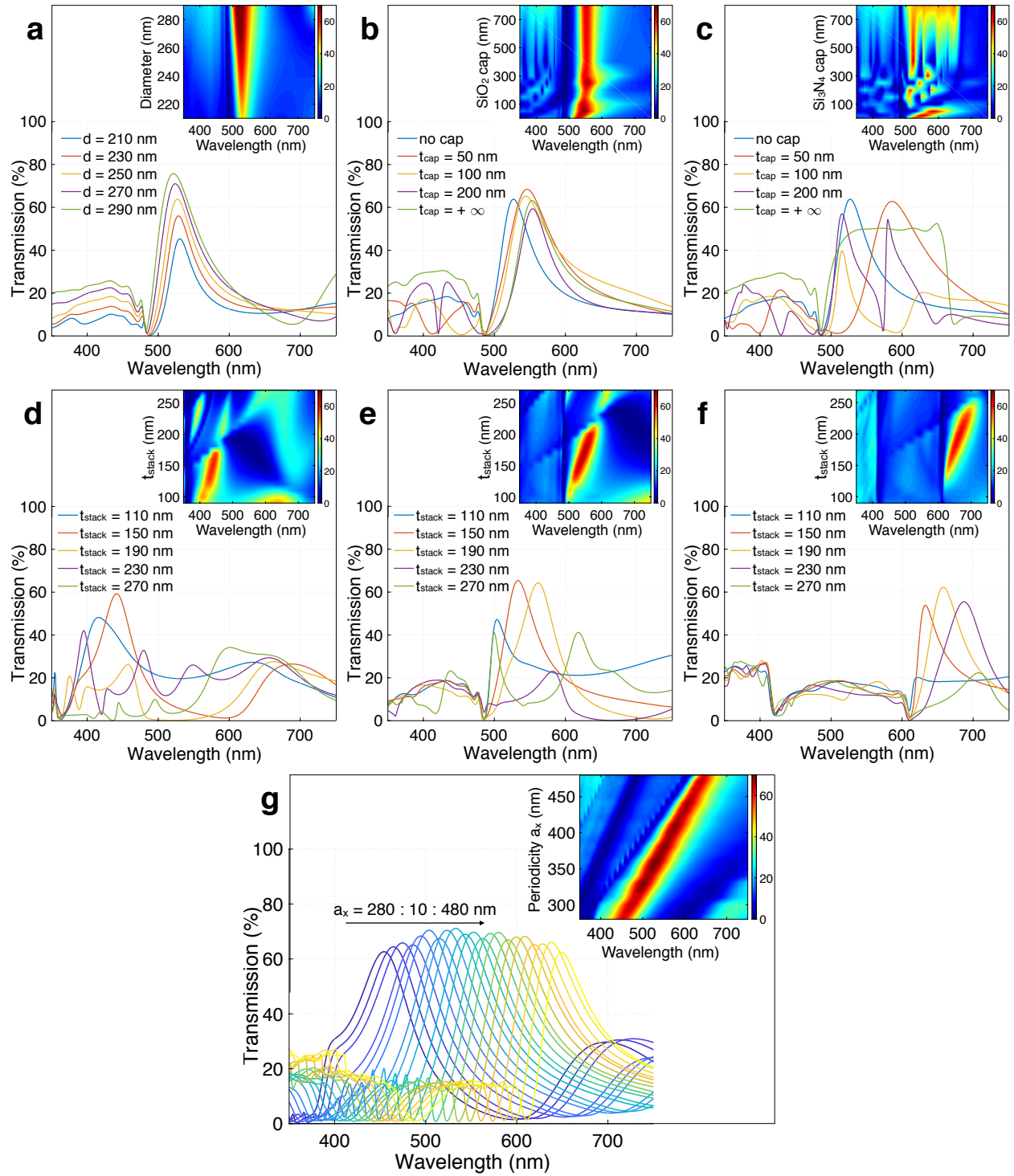


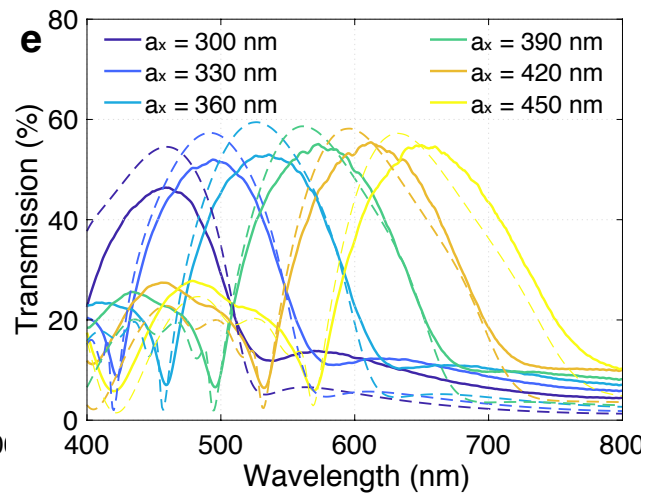
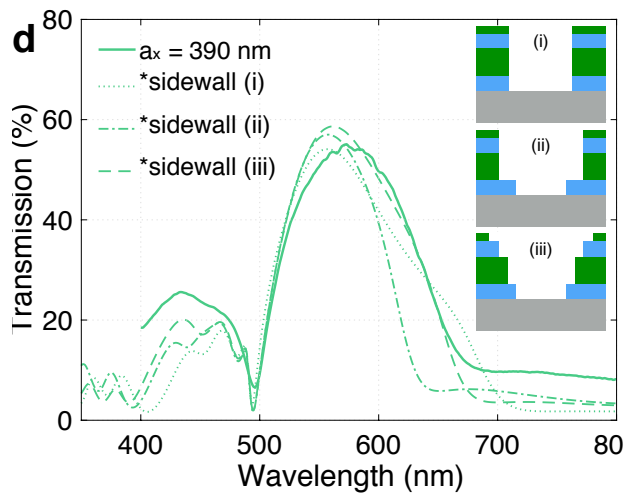
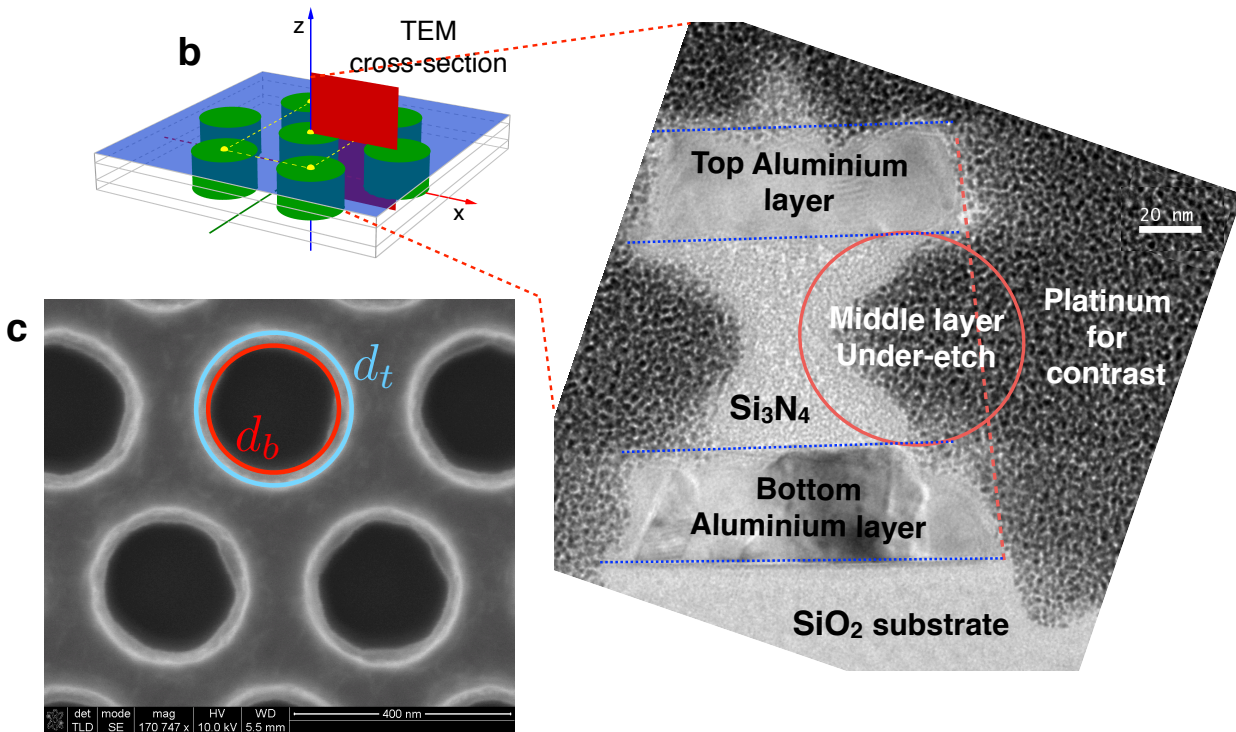
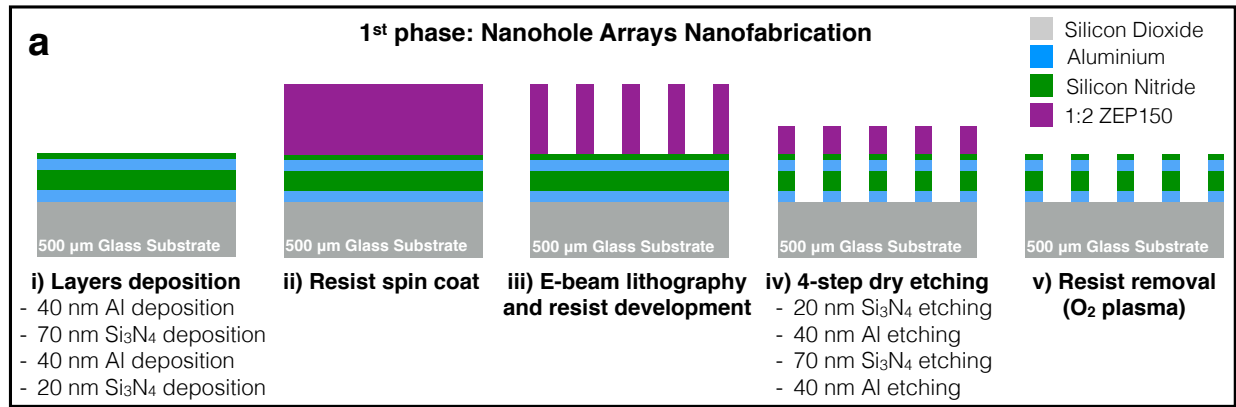
# Graphical TOC Entry



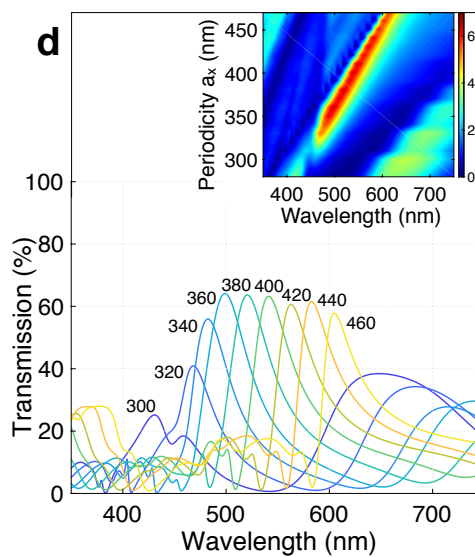
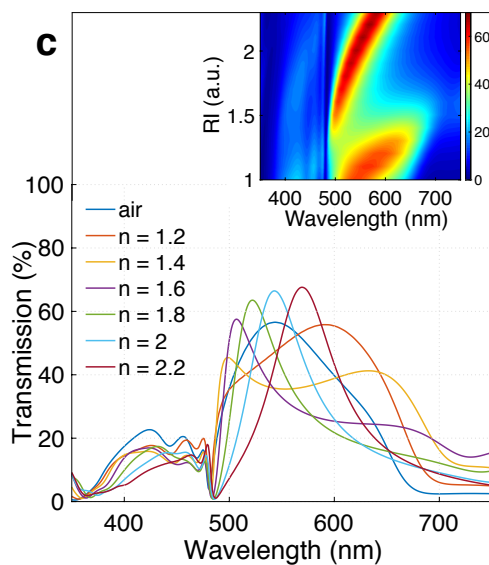
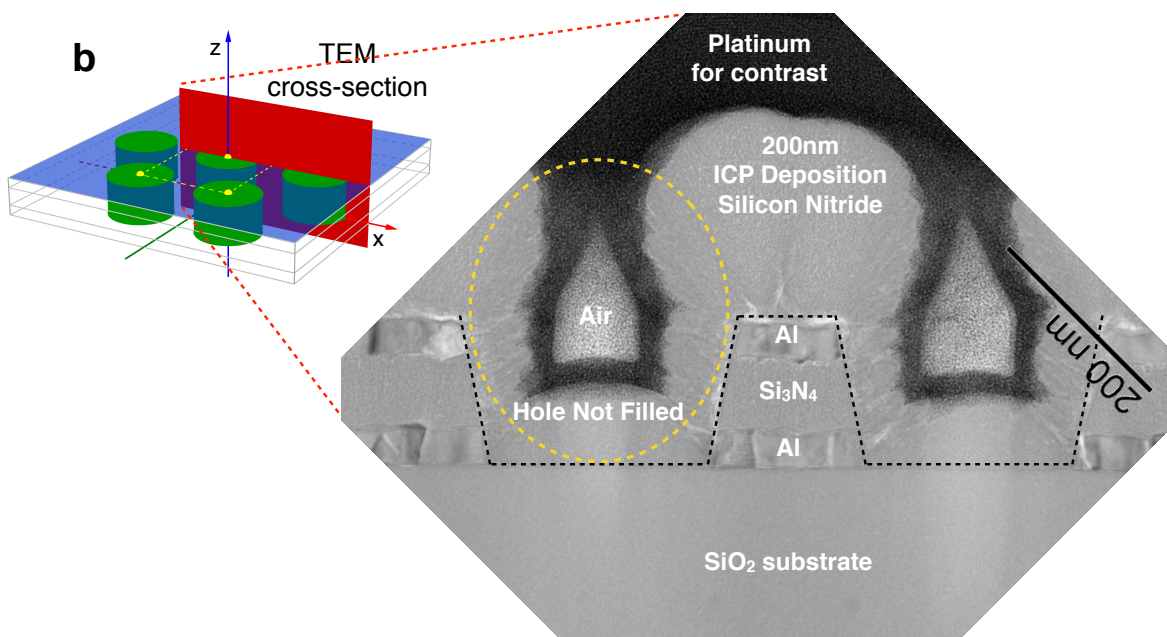
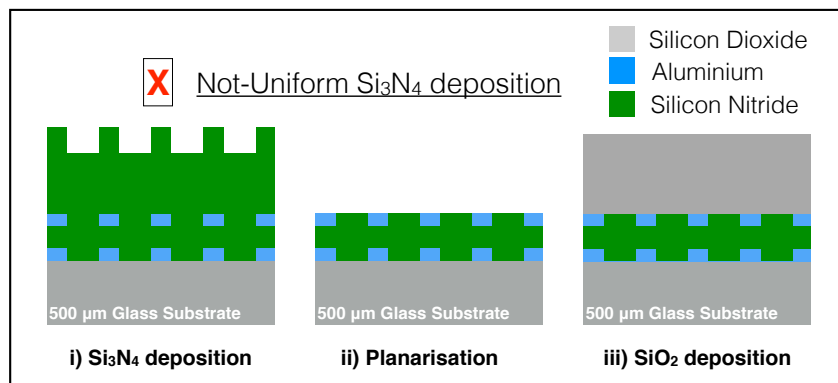








**a** 2<sup>nd</sup> phase: Si<sub>3</sub>N<sub>4</sub> hole filling





**a Alternative 2<sup>nd</sup> phase: S1805 hole filling**

